Orthogonal Gelations to Synthesize Core–Shell Hydrogels Loaded with Nanoemulsion-Templated Drug Nanoparticles for Versatile Oral Drug Delivery

Lucas Attia, Liang-Hsun Chen, and Patrick S. Doyle*

Hydrophobic active pharmaceutical ingredients (APIs) are ubiquitous in the drug development pipeline, but their poor bioavailability often prevents their translation into drug products. Industrial processes to formulate hydrophobic APIs are expensive, difficult to optimize, and not flexible enough to incorporate customizable drug release profiles into drug products. Here, a novel, dual-responsive gelation process that exploits orthogonal thermo-responsive and ion-responsive gelations is introduced. This one-step "dual gelation" synthesizes core–shell (methylcellulose-alginate) hydrogel particles and encapsulates drug-laden nanoemulsions in the hydrogel matrices. In situ crystallization templates drug nanocrystals inside the polymeric core, while a kinetically stable amorphous solid dispersion is templated in the shell. Drug release is explored as a function of particle geometry, and programmable release is demonstrated for various therapeutic applications including delayed pulsatile release and sequential release of a model fixed-dose combination drug product of ibuprofen and fenofibrate. Independent control over drug loading between the shell and the core is demonstrated. This formulation approach is shown to be a flexible process to develop drug products with biocompatible materials, facile synthesis, and precise drug release performance. This work suggests and applies a novel method to leverage orthogonal gel chemistries to generate functional core–shell hydrogel particles.

1. Introduction

Aqueous solubility has emerged as a crucial parameter to determine the bioavailability-limited efficacy of small molecule

L. Attia, L.-H. Chen, P. S. Doyle
Department of Chemical Engineering
Massachusetts Institute of Technology
77 Massachusetts Avenue, Cambridge, MA 02139, USA
E-mail: pdoyle@mit.edu
P. S. Doyle
Campus for Research Excellence and Technological Enterprise
Singapore 138602, Singapore

The ORCID identification number(s) for the author(s) of this article can be found under https://doi.org/10.1002/adhm.202301667

therapeutics. Hydrophobic active pharmaceutical ingredients (APIs) comprise an estimated 90% of candidate small molecules in the pharmaceutical development pipeline and nearly 40% of drug molecules marketed in orally-delivered drug products.[1] However, the poor bioavailability of hydrophobic APIs often prevents their translation into clinical drug products and is one of the primary causes of the failure of orally-delivered drug candidates in clinical trials.[2–5] This poor bioavailability is attributed to the slow dissolution kinetics of hydrophobic APIs in the aqueous environment of the gastrointestinal (GI) tract. Given the clinical attractiveness and higher patient compliance associated with oral delivery, enabling the oral bioavailability of hydrophobic API products has emerged as an area of active interest in the pharmaceutical industry.[6,7] Academic researchers and the pharmaceutical industry have responded by developing several solubility-enhancing formulation technologies, including milling/nanosizing and amorphous solid dispersions (ASDs), to address the limitations of poor oral bioavailability.[5,8–12] Milling or nanosizing refers to the solid handling processes that produce drug products by media-milling large API crystals to reduce crystal size.[10,13,14] This approach relies on the substantial improvement in solubility and dissolution kinetics exhibited by API crystals prepared on the nanoscale (<1000 nm). While this "top-down" approach has been employed effectively industrially to reduce crystal size, milling is energy-intensive and has been shown to introduce potentially dangerous contaminants into drug products.[2,15] ASDs, solid dispersions where the active ingredient is dispersed throughout an excipient matrix, have emerged as an alternative formulation technology.[6,16] However, ASDs can be difficult to design, because they experience physical instabilities including amorphous–amorphous phase separation and recrystallization.[7,16] Engineering long-term stability in ASDs has long been a product goal in the pharmaceutical sciences but has not been yet fully realized in practice.[17]

Biocompatible hydrogels have been widely utilized in drug product formulation to encapsulate APIs in a polymeric matrix, deliver therapeutics orally, and control drug release.[18,19] However, since hydrogels are hydrophilic in nature, they are

**ADVANCED
SCIENCE NEWS**

www.advancedsciencenews.com

**ADVANCED
HEALTHCARE
MATERIALS**

www.advhealthmat.de

incompatible to directly formulating hydrophobic APIs.[20] Numerous technologies have been developed to overcome this incompatibility and enable hydrogel formulation of hydrophobic APIs. Most notably, the incorporation of API-loaded hydrophobic nanodomains (including micelles, nanoemulsions, and lipid nanoparticles) into the hydrogel matrix has allowed for the development of high drug-loaded hydrogel formulations of hydrophobic APIs.[21–31] These hydrophobic nanodomains impart control over the formation of API nanoparticles in the polymeric matrix. This approach exploits the benefits of crystal size reduction from the bottom-up, avoiding the limitations of milling and ASDs. Additionally, using "smart," or stimuli-responsive hydrogels as the polymeric scaffold allows for the incorporation of additional functionality into the formulation, which can be exploited to access desired drug product profiles like controlled release, delayed release, targeted delivery, or immunomodulation. Clever hydrogel design can incorporate responsiveness to temperature, pH, ions, magnetic or electric fields, and biological species, among other external stimuli.[32,33]

Combination products, drug products that contain multiple APIs, have been shown to be therapeutically beneficial for clinical applications including hypertension,[34,35] diabetes, tuberculosis,[36,37] and HIV.[38,39] Specifically, fixed dosage combinations (FDCs), which contain multiple APIs in the same physical tablet or capsule, are clinically valuable to reduce patient pill burden and improve patient compliance.[40] FDCs can also unlock previously inaccessible drug product profiles, with different drug release profiles enabling therapeutic synergies. However, difficulties manufacturing FDCs have limited their clinical translation,[41–43] particularly for APIs that are compatible with different excipients.[43,44] Researchers have recently used core–shell structures as a drug product geometry that can structure drugs in distinct polymeric layers, control the release of multiple payloads, and engineer stimuli-responsive functionality.[45–50] Core–shell functionality is vital for delayed-release applications, which are important delivery routes to target enteric and colorectal diseases.[51–53] Yet, manufacturing core–shell polymeric structures typically relies on 3D printing, emulsification with an oil or lipid phase, or multi-step gelations, which have various limitations for the formulation of therapeutics for oral drug delivery.[54,55]

Here, we introduce the design of a novel dual-responsive gelation process based on biocompatible polymeric materials and nanoemulsions that is capable of simultaneous and orthogonal "dual gelations." These dual gelations rely on the orthogonal chemistries of thermoresponsive and ionotropic gelations and enable the synthesis of core–shell hydrogel particles with distinct and non-interpenetrating polymeric layers. We selected biocompatible and naturally-derived model polymers to demonstrate this approach: methylcellulose (MC) as the thermogelling polymer and alginate as the inotropic model gelator. MC has long been used as an excipient in pharmaceutical and food formulations because of its reversible thermal sol–gel behavior,[56–59] controllable erosion,[26,27,60,61] and tensioactive capabilities.[62–64] Alginate is also an ideal excipient for controlled delivery,[30,65–67] where its anionic property can protect therapeutics from being released in the gastric environment,[68–71] making alginate an optimal enteric coating.[67,72–74] Our approach overcomes the challenges of traditional solubility-enhancement approaches and exploits the advantages of "soft" templates, namely hydrogels and nanoemulsions, in the formulation and delivery of small molecule therapeutics. The resulting core–shell particles have tunable geometry that enables programmable drug release. This method requires few unit operations compared to the current state-of-the-art combination product manufacturing methods, while also structuring distinct hydrogel layers. To our knowledge, it is the first dual stimuli-responsive gelation that structures multiple hydrophobic APIs in distinct polymeric layers. The modular nature of this platform suggests that minimal adaptation can generalize this approach for the formulation of small molecule therapeutics for diverse applications in oral delivery, or for use in generating all-aqueous core–shell hydrogel particles for other applications.

2. Results and Discussion

2.1. Ions Control Thermal Gelation of Dual-Responsive Nanoemulsions

We first developed dual-responsive drug-loaded nanoemulsions by incorporating thermogelling capability from MC and ionotropic capability from $CaCl_2$ into a drug loaded-nanoemulsion. We performed a suite of rheological characterizations and analyses on the nanoemulsions to reveal the interplay between $CaCl_2$ and thermal gelation and build toward core–shell particle synthesis. We use a model hydrophobic API, fenofibrate (FEN), since it is practically water-insoluble (0.3 µg mL^{-1} at 37 °C),[75] and can benefit from nanoformulation.[76] We selected anisole as the dispersed oil phase solvent since FEN has a high saturation in anisole (0.45 g FEN/g anisole).[28] The continuous aqueous phase contains 4 wt% MC. Using ultrasonication, we synthesize a thermogelling nanoemulsion with FEN-loaded anisole nanodroplets dispersed in the continuous MC solution, as previously described.[27] We then produce dual-responsive nanoemulsions by dissolving $CaCl_2$ in the nanoemulsion at varying concentrations up to 0.09 wt% (g $CaCl_2$/g nanoemulsion, w_{CaCl_2}) (Table S1, Supporting Information). The reversible stimuli-responsiveness of the "canonical" nanoemulsion (0.06 w_{CaCl_2}) is demonstrated by the inversion test (**Figure 1**a). The first and second images show the reversible thermal sol–gel transition upon heating to 50 °C, while the second and third images show the reversible ionotropic gelation in the presence of alginate solution. We find that the presence of $CaCl_2$ in the continuous phase does not modulate the monodisperse and kinetically stable oil nanodroplet size distributions, which have a particle diameter of ≈200 nm and polydispersity index of <0.2 (Figure 1b,c).

Dual-responsive MC nanoemulsions possess interesting tunable gelation temperatures by Cl$^-$ ions. Although Cl$^-$ ions have been shown to promote gelation of MC at lower temperatures due to salting-out effects,[77,78] it is not obvious how this gel point depression is affected by the presence of nonionic surfactant and oil nanodroplets, which are present in the dual-responsive MC nanoemulsions. Through temperature ramp experiments, we characterized the gel temperature of MC solutions and the dual-responsive nanoemulsions (T_{gel}), defined as the crossover point between the loss (G'') and storage (G') moduli, as a function of w_{CaCl_2} (Figure 1d). These temperature ramp experiments clearly demonstrate that increasing w_{CaCl_2} promotes gelation at lower temperatures and results in a stronger gel for both MC

**ADVANCED
SCIENCE NEWS**

www.advancedsciencenews.com

**ADVANCED
HEALTHCARE
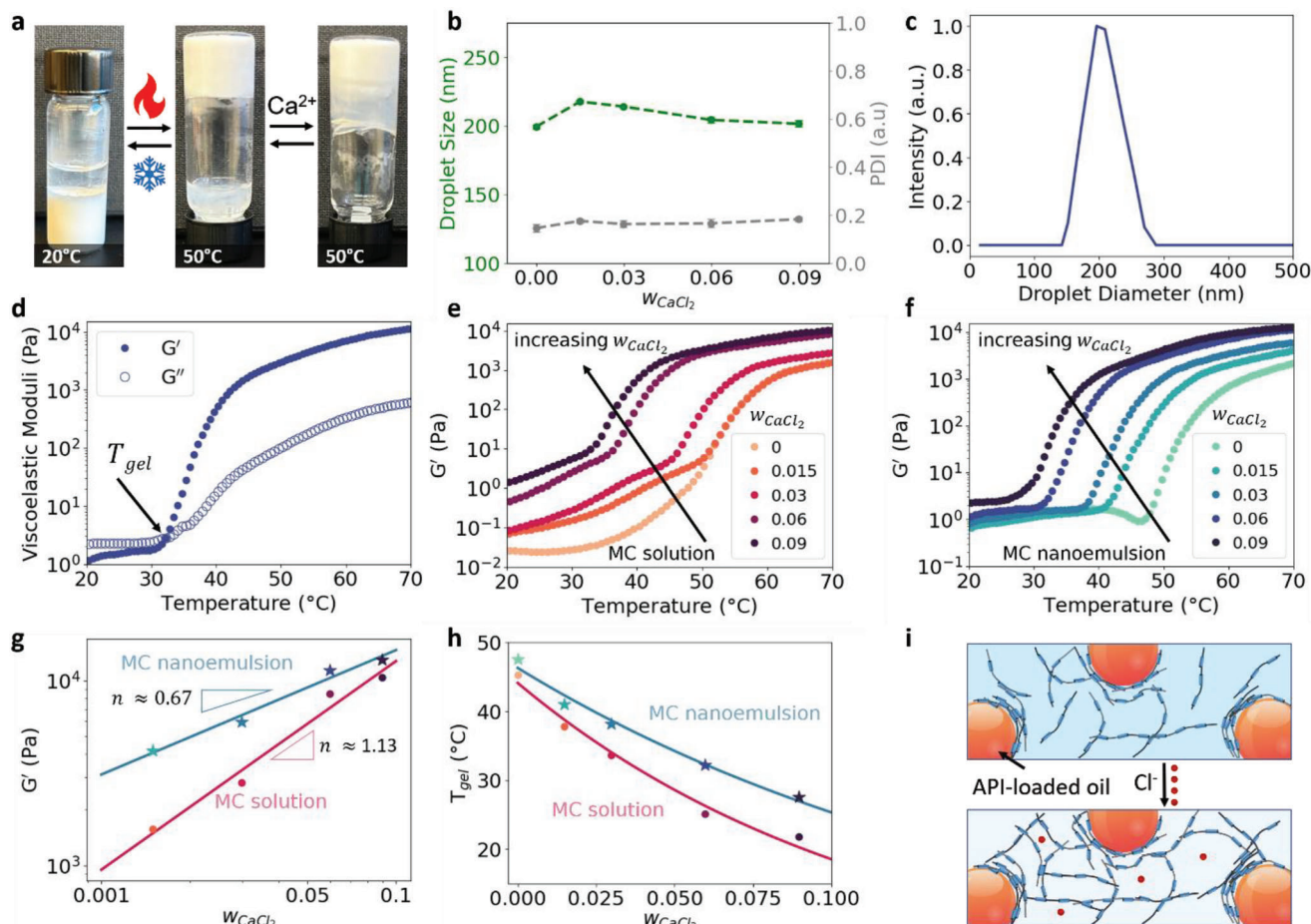MATERIALS**

www.advhealthmat.de

Figure 1. Ions control the thermal gelation of dual-responsive nanoemulsions. a) Inversion test of the nanoemulsion at temperatures of 20 and 50 °C, before and after the addition of CaCl$_2$, highlighting the thermogelation of MC nanoemulsion and the ionotropic gelation of alginate. b) The effect of w_{CaCl_2} on mean droplet size (left y-axis) and PDI (right y-axis). Y-axis error bars indicate standard deviation on mean droplet size and PDI measurements, $n = 3$. c) Representative droplet size distribution results from DLS for the canonical MC nanoemulsion. This distribution has a mean droplet size of 203.93 nm and a PDI of 0.194. d) Temperature sweep (20–70 °C) for the canonical MC nanoemulsion formulation, highlighting the gel temperature (T_{gel}) as the crossover between the loss (G'', open symbol) and storage (G', filled symbol). Temperature sweep (20–70 °C) of the effect of w_{CaCl_2} on the storage moduli G' (Pa) of 4 wt% e) MC solutions and f) MC nanoemulsions. The associated loss moduli are plotted in Figure S2, Supporting Information. g) Scaling relationships between w_{CaCl_2} and final gel strength G' (Pa). Axes are log-log, and the scaling relationship is shown as a linear regression with scaling power n. MC solution power law: $G' = 5.23 w_{CaCl_2}^{1.13}$, $R^2 = 0.99$. MC nanoemulsion power law: $G' = 4.84 w_{CaCl_2}^{0.67}$, $R^2 = 0.99$. h) Gel temperature (T_{gel}, °C) as a function of w_{CaCl_2} for MC solutions and nanoemulsions. Exponential decay is fit to each dataset. MC solution decay fit: $T_{gel} = 44.14 e^{-8.67 w_{CaCl_2}}$, $R^2 = 0.98$. MC nanoemulsion decay fit: $T_{gel} = 46.31 e^{-6.03 w_{CaCl_2}}$, $R^2 = 0.98$. i) Schematic highlighting the interplay between the salting-out effect of Cl$^-$ and surface adsorption of MC fibrils onto oil nanodroplet surfaces. The background color change indicates a decrease in solubilized MC, as MC salts out after the addition of Cl$^-$ ions.

solutions and nanoemulsions (Figure 1e,f). However, we observe different scaling of final gel strength at 70 °C (Figure 1g) and T_{gel} (Figure 1h) with w_{CaCl_2} between the MC solutions and nanoemulsions. In both cases, the MC solution exhibits a steeper scaling (increase in final gel strength, decrease in T_{gel}) with w_{CaCl_2}. Since w_{CaCl_2} was fixed for both systems, the ratio of Cl$^-$:MC is actually higher in the MC nanoemulsions than the MC solutions. However, since MC is known to be tensioactive, some MC polymers localize on the oil nanodroplet surface.[63,79,80] The sequestering of MC onto the oil nanodroplet surface suggests that the salting-out phenomena will have a dampened effect compared to an MC solution, which we observe experimentally. We schemat-

ically show the hypothesized competition between the salting-out phenomena and the surface adsorption of MC polymers in Figure 1i. In the inter-droplet regions, the addition of Cl$^-$ induces the salting-out effect. In contrast, the surface-adsorbed MC experiences a smaller change in network density and MC hydrophobic association. This competition between salting-out and MC surface adsorption produces different rheological scaling. At the highest w_{CaCl_2} (0.09 wt%), T_{gel} is driven down to 21.82 and 27.63 °C from 45.28 and 47.60 °C when no salt is added, for MC solutions and nanoemulsions, respectively. This substantial decrease in T_{gel} suggests that this formulation approach could be utilized even for thermally labile APIs.
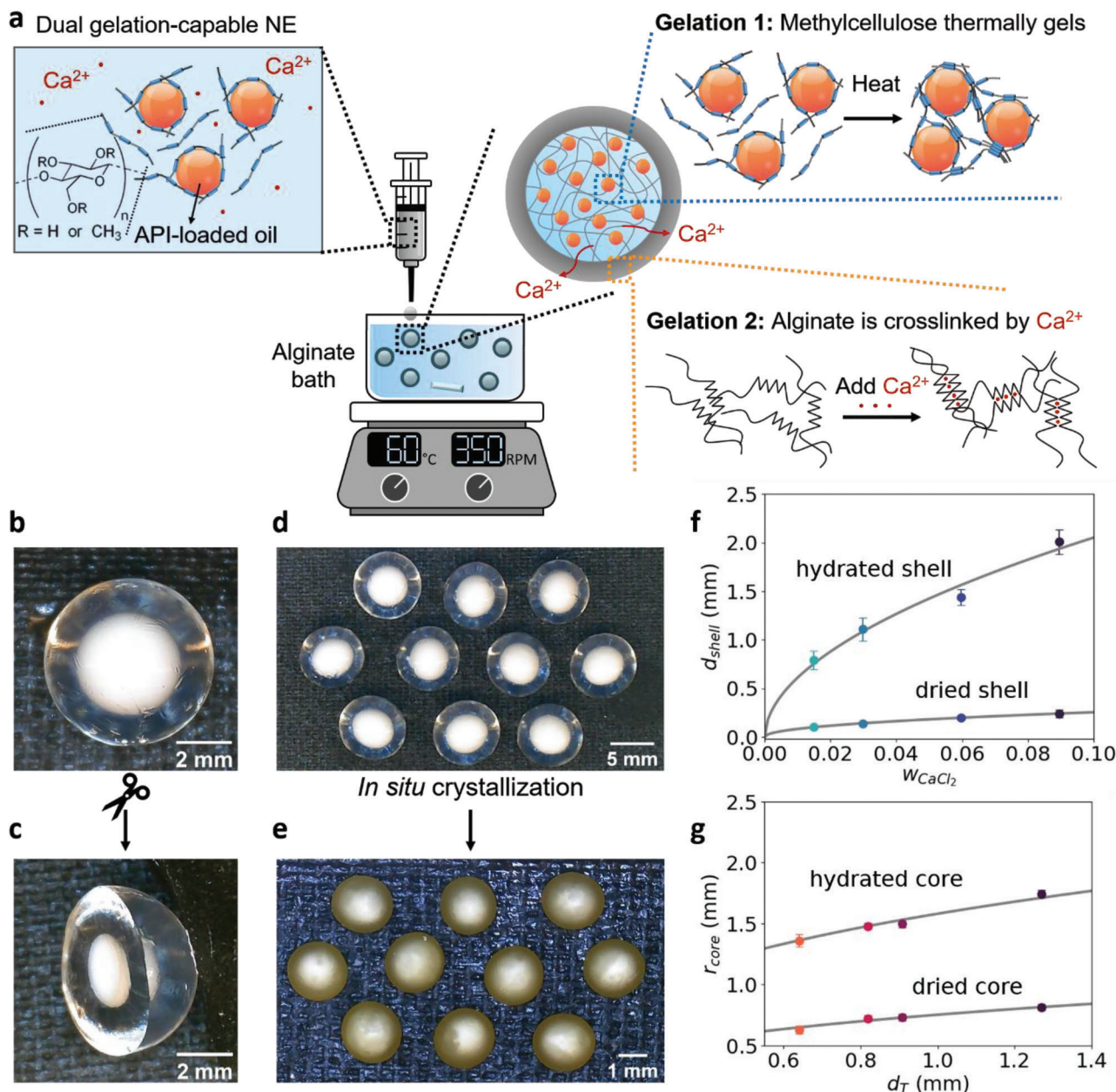
Figure 2. Orthogonal gelations synthesize core–shell hydrogel particles with tunable geometry. a) Schematic describing the simultaneous dual gelation dripping method. The dual gelation-capable nanoemulsion (NE) is dripped through a syringe needle into a heated alginate bath. The MC drop thermally gels upon contact with the heated bath, while Ca^{2+} ions diffuse from the gel core and crosslink alginate polymers in the bath, forming the gel shell. b) Digital microscopy image of "canonical" particle, c) which is halved with a surgical blade to visualize the clean interface between gel layers. Scale bar is 2 mm. Digital microscopy images of d) hydrated and e) dried particles from the "canonical" formulation. Scale bar is 5 mm for (d) and 1 mm for (e). Images of other particles are shown in Figure S3, Supporting Information. f) Power law scaling of d_{shell} with w_{CaCl_2}. Hydrated shell power law (blue): $d_{shell} = 6.92w_{CaCl_2}^{0.527}$, $R^2 = 0.97$. Dried shell power law (red): $d_{shell} = 0.79w_{CaCl_2}^{0.490}$, $R^2 = 0.99$. Y-axis error bars represent the standard deviation of d_{shell} measurement, $n = 10$. g) Power law scaling of r_{core} with d_T according to Tate's law for designing particle size. Hydrated shell Tate's law (blue): $r_{core} = 1.58d_T^{1/3}$, $R^2 = 0.98$. Dried shell power law (red): $r_{core} = 0.75d_T^{1/3}$, $R^2 = 0.96$. Y-axis error bars represent the standard deviation of r_{core} measurement, $n = 10$.

2.2. Orthogonal Gelations Synthesize Core–Shell Hydrogel Particles with Tunable Geometry

After preparing and characterizing the dual-responsive MC nanoemulsions, core–shell particles were synthesized using the dual gelation process, sketched schematically in **Figure 2**a. This schematic highlights how the simultaneous gelations occurring through orthogonal gelation mechanisms result in a core–shell hydrogel particle. The dual-responsive MC nanoemulsion is dripped from a syringe needle into a heated alginate bath.

**ADVANCED
SCIENCE NEWS**

www.advancedsciencenews.com

**ADVANCED
HEALTHCARE
MATERIALS**

www.advhealthmat.de

While the comparatively fast thermogelation immobilizes oil nanodroplets in the MC network and produces a composite MC hydrogel core layer, Ca^{2+} diffuses from the core to crosslink free alginate polymers in the bath, producing the alginate hydrogel shell layer. The sharp interface between the core and shell gel layers can be observed in Figure 2b,c, which shows a single canonical core–shell particle, which is then cut in half in order to visualize the interface between the MC and alginate gels. The opaque MC core and translucent alginate shell gel layers are successfully distinct and non-interpenetrating. We hypothesize that the sharp interface results from the relative timescales of each gelation mechanism. In a scaling analysis, we show that the MC droplet surface gels faster (≈10 ms) than the diffusion timescale of alginate polymers, suggesting that these relative timescales give rise to the sharp interface between gel layers (Section S3, Supporting Information). After synthesis, we collect the core–shell hydrogel particles (Figure 2d) and perform a drying step at 70 °C to evaporate the anisole and water, generating FEN nanocrystals embedded in composite core–shell particles. The dried composite core–shell particles (Figure 2e) are then harvested for solid-state characterization.

We characterized the dual gelation process in terms of two formulation parameters: the outer diameter of the dispensing tip (d_T) and w_{CaCl_2} in the thermogelling nanoemulsion. We hypothesized that we could achieve independent control over the geometry of the core and shell layers by modulating these two formulation parameters. The design space for d_T was varied between 23 and 18 G needles, while w_{CaCl_2} was varied between 0.015 and 0.09 w_{CaCl_2}, based on previous studies of alginate gelation kinetics.[81] When varying w_{CaCl_2}, the tip size was fixed at 18 G. When varying the tip size, w_{CaCl_2} was fixed at 0.006 w_{CaCl_2}. These two parameter values describe the canonical formulation condition. The synthesized core–shell particles were characterized in terms of the radius of the MC core (r_{core}) and the thickness of the alginate shell (d_{shell}), for both hydrated particles and dried particles. We observed that d_{shell} scales with w_{CaCl_2} (Figure 2f), since Ca^{2+} corresponds to a stronger driving force for ionotropic gelation. We also found that r_{core} scales with $d_T^{1/3}$ (Figure 2g), following Tate's design law for droplet size,[82] shown in Equation (S5), Supporting Information. Section S4, Supporting Information, summarizes additional particle size analyses that support the use of w_{CaCl_2} and d_T as design parameters that can independently tune d_{shell} and r_{core}, respectively.

These results suggest that a wide range of particle geometries are synthesizable from this manufacturing method, expanding the types of applications for which these core–shell particles could be utilized. For example, since particle geometry influences the drug release behavior and performance, independent control over d_{shell} and r_{core} enables tunable release profiles, as explored in Section 2.4. This all-aqueous dual gelation confers advantages over other core–shell particle synthesis approaches. Particularly, many techniques rely on microfluidic emulsification, which requires an oil or lipid sheathing solvent such as in refs.[83,84]. For subsequent formulation or delivery of these particles, removing particles from the oil solvent can require expensive extraction operations. In contrast, this dual gelation approach uses a biocompatible hydrogel shell formed from an aqueous bath, enabling a simple extraction step prior to drying.

2.3. In Situ Crystallization Templates Drug Nanocrystals in the Methylcellulose Matrix

After performing in situ crystallization, vaporizing water, and anisole (**Figure 3**a), we characterized the composite MC-FEN particle core using a suite of solid-state techniques. Previous work has demonstrated that an encapsulated FEN nanoemulsion successfully templated drug nanocrystals embedded in the MC matrix.[27] Here, we find that drug nanocrystals are successfully templated through solvent extraction, and we report the discovery of polymer-drug coating which results in faceted composite granules, discussed in greater detail in Section 2.4.

Comparing the X-ray diffraction (XRD) pattern of the composite FEN against bulk FEN (as received), we observe the characteristic peaks of FEN's stable crystalline form 1 polymorph at diffraction angles ($2\text{-}\theta$) of 12°, 14.5°, 16.2°, 16.8°, and 22.4° (Figure 1b).[85] The Raman spectra also exhibit characteristic FEN form 1 polymorph peaks, as marked in Figure 1c. DSC thermograms demonstrate melting point depression between the bulk FEN (81.63 °C) and composite MC-FEN samples (76.54 °C), with $\Delta T = 5.09$ °C (Figure 1d). This melting point depression paired with the confirmation that the FEN is crystalline supports the successful formation of FEN nanocrystals within the MC matrix. Using a previously determined correlation between fusion enthalpy and melting temperature,[86] we estimate a degree of crystallinity of $\approx100\%$ for the composite MC-FEN, suggesting nearly all of the FEN is successfully crystallized (Section S5, Supporting Information). Comparing estimates for nanocrystal size, we find that a mass balance on the oil droplet yields $d_{crystal} = 150.1$ nm, while TEM imaging of individual nanocrystals yields $d_{crystal} = 175.9 \pm 53.5$ nm, showing strong agreement (Section S6, Supporting Information). The drug loading (w FEN/w core) was predicted using the approach described in Section S7, Supporting Information, and the analytical drug loading of the core was measured at 49.8% (Figure 3e). Nearly all of the drug should be encapsulated in the particle since the significant solubility difference of FEN in water versus anisole suggests that the drug will not partition out of the anisole droplets, as demonstrated analytically in ref. [27]. The distinct core and shell layers and the sharp interface between the polymeric layers are clearly visible in the high-resolution scanning electron microscopy (SEM) micrograph shown in Figure 3f. Since the alginate shell is unloaded, the surface is uniform and undisturbed (Figure 3g). Faceted structures with a characteristic length scale of ≈1 μm uniformly dominate the topology of the composite core (Figure 3h). While these structures are faceted, the measured drug loading (49.8%) suggests that these structures are polymer-coated FEN granules with tightly surface-adsorbed MC, since by mass balance they cannot be purely drug crystals. The microstructure and morphology of the composite MC-FEN granules are further explored in Section 2.4 and Section S11, Supporting Information.

Here, we present a facile method to manufacture nanocrystals from nanoemulsion templates and stabilize the nanocrystals within an MC matrix. This bottom-up method can provide direct control over nanocrystal size through the size of the oil nanodroplet templates. In contrast to top-down manufacturing approaches that require milling, this approach is comparatively gentle and simpler to optimize. This method also provides direct control over the drug loading in the particle by tuning ϕ_{oil}
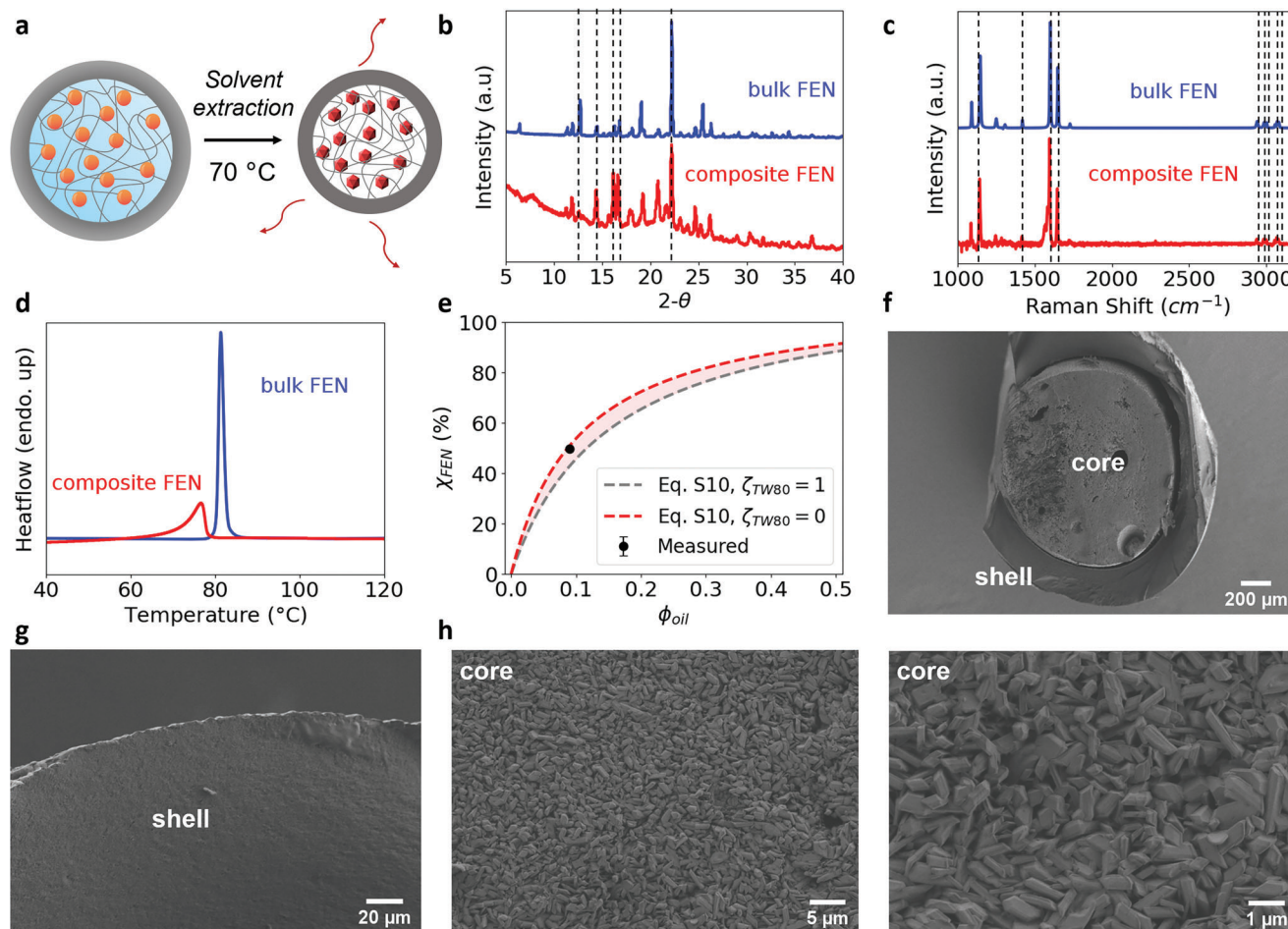
Figure 3. In situ crystallization templates drug nanocrystals in the MC matrix. a) Schematic describing the solvent extraction from hydrated particles to dried particles. Volatile anisole and water are evaporated, templating FEN nanocrystals in the MC matrix surrounded by an alginate polymeric layer. b) XRD pattern and c) Raman spectra for bulk FEN and composite MC-FEN particle (core). Characteristic peaks for the crystalline form I FEN are indicated using the overlaid dashed lines. d) DSC thermograms for bulk FEN and composite MC-FEN particles. Endothermic heat flow is shown in the positive y-axis direction. Temperature (°C) is shown on the x-axis. e) Drug loading content of the particle core (χ_{FEN}) as a function of oil volume fraction (ϕ_{oil}) in the nanoemulsion. The red dashed curve corresponds to Equation (S12), Supporting Information, with $\zeta_{TW80} = 0$ (complete Tween 80 removal). The gray dashed curve corresponds to Equation (S12), Supporting Information, with $\zeta_{TW80} = 1$ (complete Tween 80 retention). For both curves, $\zeta_{CaCl_2} = 0$ (complete CaCl$_2$ removal). The black point corresponds to measured drug loading content. Y-error bars correspond to standard deviation, with $n = 3$. SEM micrographs of the canonical particle f) halved with a surgical knife to view the interior microstructure of the core and the shell, g) the alginate shell layer, and h) dominant surface topology of the MC-FEN composite core. Scale bars for (f), (g), and (h) are 200 µm, 20 µm, 5 µm (left), and 1 µm (right), respectively.

in the nanoemulsion. Crystallizing API inside an excipient matrix (so-called "co-processing"), can enable excipient-stabilized nanocrystals.[7,87] In sum, this approach can be a scalable method to manufacture drug nanocrystals.

2.4. Delayed Pulsatile Drug Release Can Be Programmed from Formulation Parameters

We demonstrate programmable delayed pulsatile drug release from the core–shell particles in a biorelevant release media for the range of particle formulations. First, we observe that the nanocrystalline formulation of FEN exhibits a substantial improvement in the release rate of FEN compared to the bulk FEN crystals (gray curve in **Figure 4**a). The bulk FEN takes 8.6 h to

reach 80% release and 19.6 h to reach complete release, while the nanocrystalline FEN takes 0.5 h to reach 80% and 0.8 h to reach complete release after the programmed release point. We also establish facile control over the release profile using the key formulation parameters w_{CaCl_2} and d_T (Figure 4a,b). We observe that the programmed release point (t_{lag}, defined in Figure 4c) increases substantially with increasing w_{CaCl_2} (Figure 4a). This is intuitive as increasing w_{CaCl_2} corresponds to a thicker alginate shell which takes longer to degrade and allow release from the core. Similarly, we observe that t_{lag} slightly increases as d_T increases, since increasing d_T corresponds to larger particles which take longer to degrade. For both experiments, the release "suppression" is effective, with minimal drug release from the particles until t_{lag}. To develop a predictive model for programmed release, we hypothesized that t_{lag} could account for the variability in the release
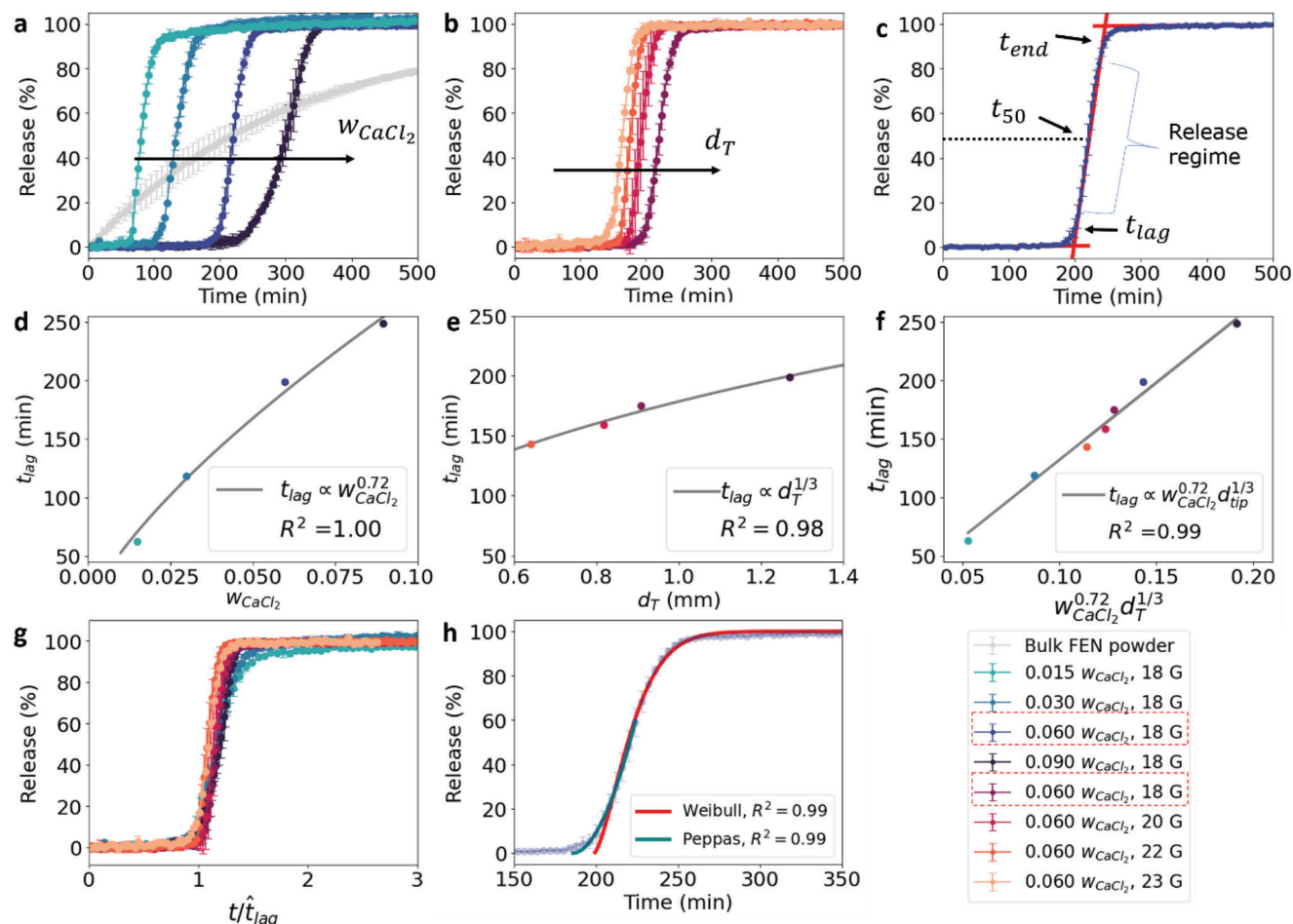
Figure 4. Delayed pulsatile drug release can be programmed from formulation parameters. Drug release profiles for a) varied w_{CaCl_2} experiment and b) varied d_T experiment. Curves from left to right indicate increasing w_{CaCl_2}. Dissolution curves show every third point plotted for ease of visualization. Y-axis error bars indicate the standard deviation of experimentally calculated dissolution proportion, $n = 3$. Legend is provided for reference, with the canonical formulation circled with red dotted lines. c) Drug release profile for the canonical formulation. Characteristic time scales (t_{lag}, t_{50}, t_{end}) of the dissolution profile are labeled. Additionally, the labeled release regime indicates when the drug is actively solubilized from the particles. d) t_{lag} plotted as a function of w_{CaCl_2}. Power law fit $t_{lag} = 1.43e3 w_{CaCl_2}^{0.72}$, $R^2 = 0.99$. e) plotted as a function of d_T. Power law fit $t_{lag} = 257.14 d_T^{1/3} - 78.56$, $R^2 = 0.98$. f) t_{lag} plotted against the linearized process variables using the power law scaling from (d) and (e). Linear fit: $\hat{t}_{lag} = 1.32e3 w_{CaCl_2}^{0.72} d_T^{1/3}$. g) Dimensionless release profiles rescaled using the model for $\hat{t}_{lag}$. This rescaling collapses all release profiles to a master design curve. h) Dissolution profile for the canonical formulation. The Weibull ($R^2 = 0.99$) and Peppas or power law ($R^2 = 0.99$) models are fit to the dissolution data. The best-fit model parameters are summarized in Tables S4 and S5, Supporting Information.

profiles, since t_{lag} exhibits a dependence on both process parameters. We thus quantified the scaling of t_{lag} with w_{CaCl_2} and d_T, where t_{lag} scales with w_{CaCl_2} according to the cross-linking density and with d_T according to a modified Tate's law, as shown below in Equation (1)

$$\tau \propto k d_T^{\frac{1}{3}} \tag{1}$$

where τ describes the characteristic timescale and k is a fit constant (Figure 4d,e, other characteristic timescales are shown in Figure S9, Supporting Information). Using these scaling relationships, we developed a linearized model for predicted t_{lag} ($\hat{t}_{lag}$), shown in Figure 4f. The release profiles for both experiments are

then rescaled by $\hat{t}_{lag}$, which collapses all release profiles onto a master curve that describes the release as a function of dimensionless time ($t/\hat{t}_{lag}$) for a given process condition (Figure 4g).

The Peppas (power law) model[88] and the Weibull model[89] were then fit into the drug release data to gain insight into the mechanism of drug release. Figure 4h highlights the fits for these models on the dissolution data for the canonical formulation. The Peppas model fit yields a diffusional coefficient between 1.18 and 1.92 for all formulations (Table S4, Supporting Information), suggesting a drug release mechanism of Super Case II transport, which is consistent with other studies of release from cellulose-based matrices.[27,88] This is corroborated by the fitted exponent for the Weibull model, which ranges between 1.01 and
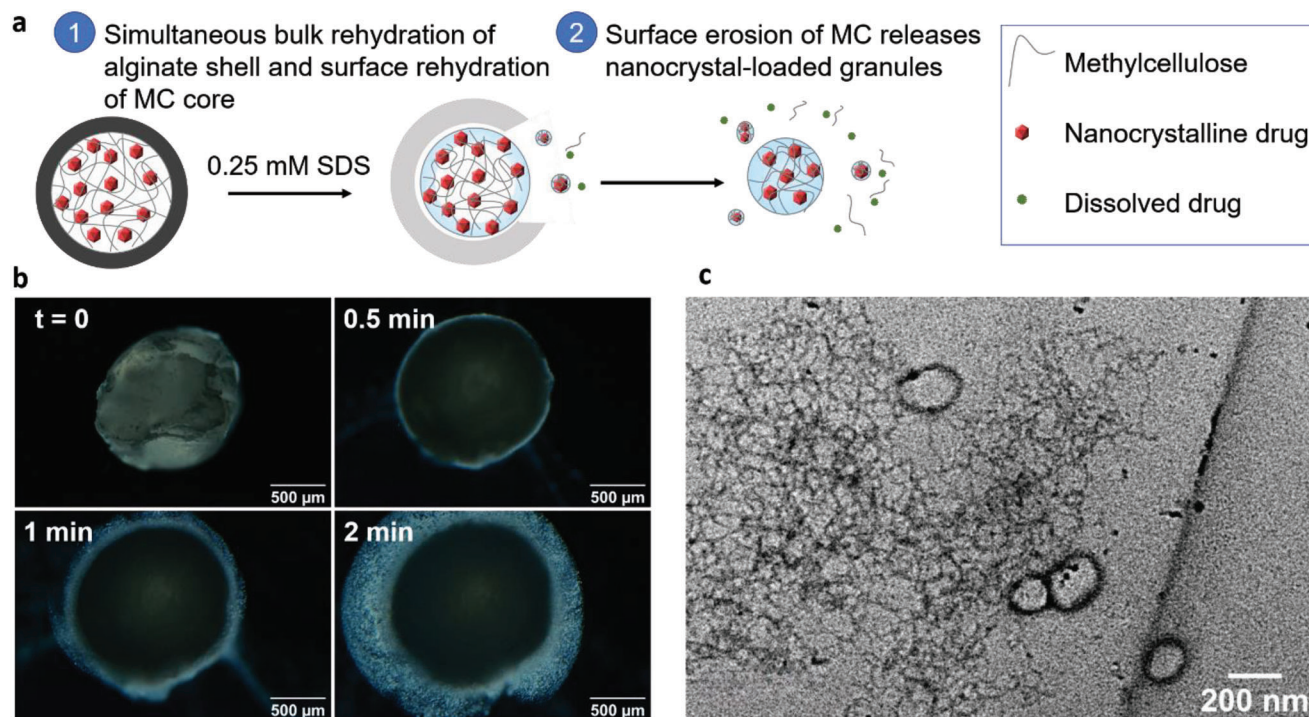
Figure 5. MC-coated FEN nanocrystals erode from the surface of the composite core. a) Schematic of the proposed drug release mechanism. b) Cross-polarized micrographs of composite MC-FEN core dissolution. Surface erosion of the core releases "microgranules" containing FEN nanocrystals, which then dissolve. Scale bar is 500 µm. c) Representative TEM micrographs of redispersed composite MC-FEN core. FEN nanocrystals ($d_{crystal} = 175.9 \pm 53.5 nm$, $n = 10$) can be seen embedded in a dispersed MC fibril network. Scale bar is 200 nm.

1.74 (Table S5, Supporting Information), suggesting that the release mechanism is not controlled by diffusion, but by matrix erosion.[89] Since the release mechanism is erosion-controlled, we hypothesized that for increasing d_T, the peak release rate of FEN would decrease since this corresponds to an increase in r_{core}. However, as shown in Figure S10, Supporting Information, the peak release rate did not increase monotonically with decreasing r_{core}, but stays relatively constant. This result is explained by the release mechanism, as discussed in Section S10, Supporting Information, and below in **Figure 5**.

Compared to other core–shell particle synthesis approaches, this dual gelation has easily tunable release kinetics through the control of particle geometry, which is important for applications in controlled release. For example, a recent approach used electrospraying to synthesize polyvinylpyrrolidone K10 (PVP)-shellac core–shell particles and demonstrated a release suppression of 2 h in pH-2 media.[90] However, it was not determined what controls the shellac degradation timescale, or whether this timescale can be independently tuned during the electrospraying process. Another technology that utilized co-axial prilling to synthesize an alginate shell was unable to prevent drug release through the alginate shell, and could only reduce the release rate rather than delay release.[91] In contrast, this dual gelation approach provides a route for facile control over the delayed release timescale, with strong release suppression and minimal drug leakage.

The strong release suppression reported in these results suggests that these core–shell particles could be widely applicable in oral delayed and sustained release applications. The programmability of the release based on simple scaling with process parameters highlights how this platform can access a diverse range of drug product profiles. We demonstrate release suppression between 1 and 4 h, which correlates well to in vivo residence time of drug products in the stomach (5 min–1 h)[92,93] and the small intestine (3–4 h).[51,94] The tunability of this release suppression timescale suggests that this approach could be suitable to target delayed pulsatile enteric or colonic release, ensuring a therapeutic is protected from the gastric environment. Oral drug delivery systems with this delayed pulsatile release behavior could also be useful in treating disease processes that exhibit circadian rhythms in their pathology, so-called "chronotherapy."[95–97] Simple mixtures of particles with different suppression timescales in a multi-particulate formulation could enable sustained-release functionality to reduce pill burden, an important clinical challenge in chronic disease.[98]

After performing dissolution testing and analysis, we investigated the release mechanism. The schematic depicted in Figure 5a demonstrates the proposed two-step drug release mechanism. The core–shell particles are first rehydrated in solution, where the alginate shell undergoes bulk rehydration, while MC experiences surface rehydration, as described in ref.[99]. The alginate shell undergoes bulk erosion via ion displacement, where Na^+ competes with Ca^{2+} in the matrix and weakens the gel structure,[100] until it ruptures and releases the MC core. Next, the composite granules erode from the MC surface and the nanocrystalline FEN solubilizes. We reproduce this release mechanism in a kinetic study of particle rehydration and dissolution, and we find that the time at which the alginate shell ruptures is close to t_{lag} (Figure S11, Supporting Information). A
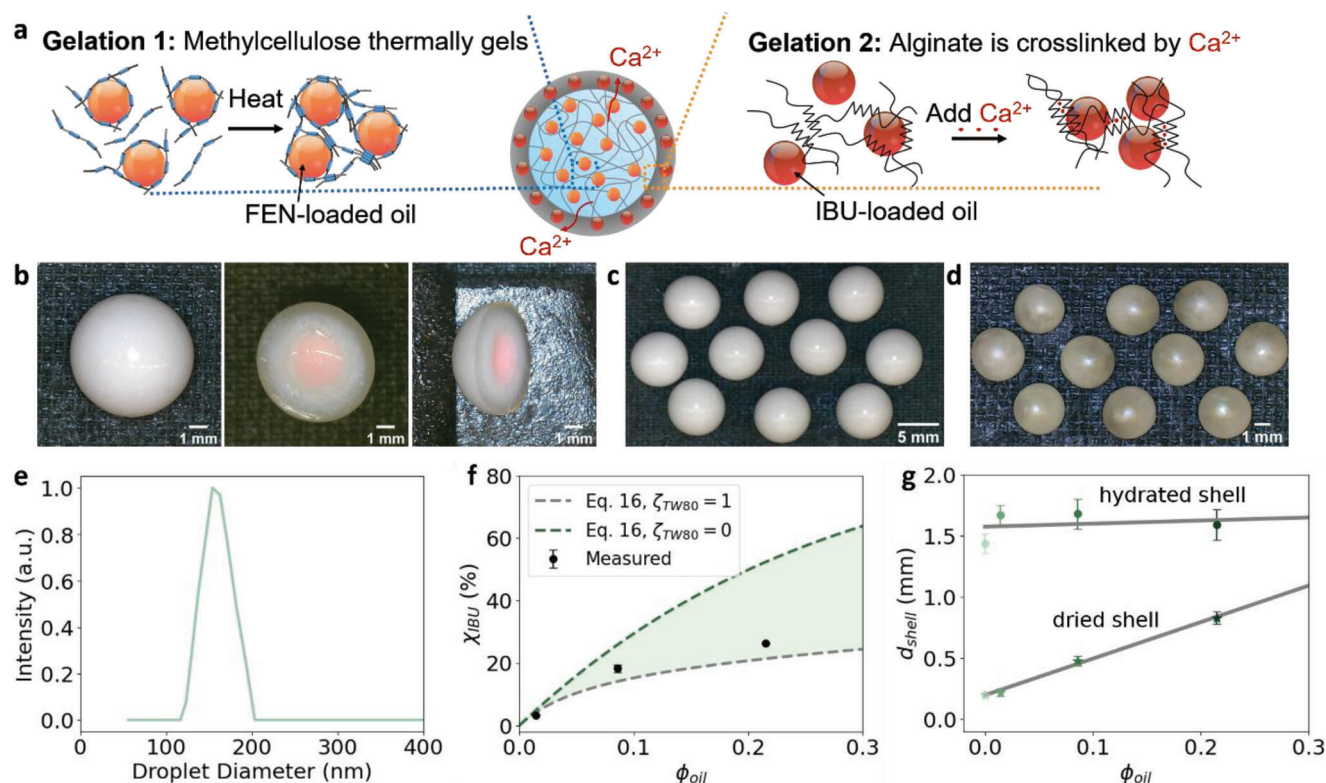
**ADVANCED
SCIENCE NEWS**

www.advancedsciencenews.com

**ADVANCED
HEALTHCARE
MATERIALS**

www.advhealthmat.de

Figure 6. Combination particles encapsulate two drug-loaded nanoemulsions. a) Schematic showing FEN and IBU loading in core and shell for combination particle synthesis using dual gelation. Digital microscopy images of a representative hydrated IBU-FEN combination particle with b) Nile red dye loaded into the oil phase of the MC-FEN nanoemulsion. Scale bar is 1 mm. Digital microscopy image of IBU-FEN combination particles (alg-IBU shell, MC-FEN core) at the middle loading level, $\phi_{oil} = 0.09$, with c) hydrated and d) dried particles. Scale bar is 5 and 1 mm for (c) and (d), respectively. e) Representative droplet size distribution results from DLS for the IBU-loaded alginate nanoemulsion (alg-IBU). This distribution has a mean droplet size of 178.57 nm and a PDI of 0.24. f) Predicted and measured drug loading (by mass) for IBU in the alginate shell. The green curve represents Equation (S16), Supporting Information, with $\zeta_{TW80} = 0$ (complete Tween 80 removal). The black curve represents Equation (S16), Supporting Information, with $\zeta_{TW80} = 1$ (complete Tween 80 retention). UV–vis calibration is reported in Figure S14, Supporting Information. The black points show measured drug loading for each ϕ_{oil} level. Error bars represent standard deviation in drug loading, $n = 3$. g) Hydrated and dried d_{shell} plotted against ϕ_{oil} for unloaded shells and the three shell loading levels. Error bars represent the standard deviation in d_{shell}, $n = 10$. Linear best fits are shown for the hydrated and dried shells. Fit for hydrated shells $d_{shell} = 0.25\phi_{oil} + 1.58$, $R^2 = 0.22$. Fit for dried shells $d_{shell} = 2.99\phi_{oil} + 0.20$, $R^2 = 1.00$.

simulated surface erosion experiment, in which we dripped release media onto an extracted core to erode the surface, confirms that crystalline-containing granules erode from the MC surface and indicates that nanocrystalline FEN is released before it is solubilized (Figure 5b). These granules have a median granule size of 2.25 ± 0.84 µm ($n = 84$), as determined from brightfield microscopy (Figure S12, Supporting Information). To confirm that these granules were polymer-drug composites, we directly imaged FEN nanocrystals using TEM. The micrograph in Figure 5c depicts spheroidal FEN nanocrystals embedded in a semi-eroded MC matrix. The nanocrystal size distribution measured by TEM closely matches predictions based on the oil nanodroplet size distribution, as discussed in Section S6, Supporting Information.

The discovery of tightly surface-adsorbed MC-FEN granules suggests interesting molecular interactions during crystallization. Previous work has supported this observation, since the unsubstituted hydroxyl groups of MC are capable of hydrogen bonding, and FEN has four hydrogen bond acceptors.[101,102] Molecular simulations have shown that MC and HPMC have a strongly favorable energetic interaction with surfaces of hydrophobic APIs,

including FEN, through hydrogen bonding.[103–106] Controlling intermolecular interactions during crystallization within hydrogel scaffolds could present an opportunity for polymorphic control, a long-desired goal of drug substance manufacturing.[107]

2.5. Combination Particles Encapsulate Two Drug-Loaded Nanoemulsions

We extended this core–shell synthesis platform to demonstrate manufacturing combination products with different drugs structured in the core and shell. To accomplish this, a second drug-loaded nanoemulsion was loaded into the alginate bath, such that the oil nanodroplets would be encapsulated in the shell during the alginate crosslinking (**Figure 6**). Ibuprofen (IBU) was selected as a second model hydrophobic therapeutic, but this approach can generalize to other hydrophobic APIs loaded into a nanoemulsion. We synthesized IBU nanoemulsion at three different oil volume fractions ($\phi_{oil} \in \{0.01, 0.09, 0.21\}$) to demonstrate variable drug loading of the shell as independent from the
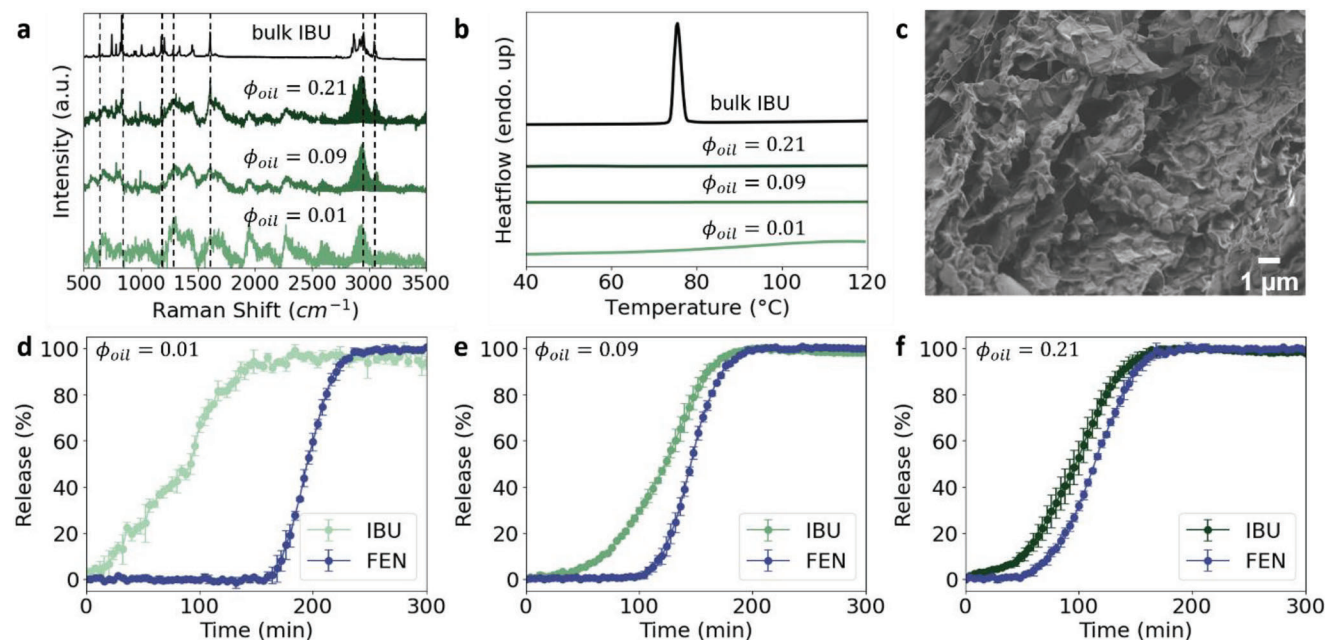
**ADVANCED
SCIENCE NEWS**

www.advancedsciencenews.com

**ADVANCED
HEALTHCARE
MATERIALS**

www.advhealthmat.de

Figure 7. Combination particles enable tunable sequential release. a) Raman spectra for bulk IBU and composite alg-IBU particle shell. Characteristic peaks for amorphous IBU are indicated with dashed lines. b) DSC thermograms for bulk IBU and composite alg-IBU shell. Endothermic heat flow is shown in the positive *y*-axis direction. Temperature (°C) is shown on the *x*-axis. c) SEM micrograph of the dried alginate matrix loaded with amorphous IBU at the high loading level. Amorphous IBU particles can be observed embedded in the alginate matrix. Scale bar is 1 μm. Drug release from the combination particles with both IBU release from the shell (green) and FEN release from the core (blue) for (d) low IBU loading ($\phi_{oil} = 0.01$), (e) middle IBU loading ($\phi_{oil} = 0.09$), and (f) high IBU loading ($\phi_{oil} = 0.21$). Dissolution curves show every third point plotted for ease of visualization. *Y*-axis error bars indicate the standard deviation of experimentally calculated drug release, $n = 3$.

drug loading in the core. More details on the design of this nanoemulsion are included in Section S12, Supporting Information, and the full formulation parameters are summarized in Table S5, Supporting Information. We used the canonical formulation for the MC-FEN nanoemulsion in the core.

Unlike the clear alginate shells displayed in Figure 2b–d, the shells of these combination particles are opaque, since the encapsulated nanoemulsion scatters visible light (Figure 6b–d). Some particles were synthesized with a red dye (Nile red) loaded into the oil phase of the MC nanoemulsion as a contrast agent, and the gel interface between the core and the shell is easily visible (Figure 6b). We designed the IBU nanoemulsion to have a similar droplet size distribution as the dual-responsive MC-FEN nanoemulsion, and we indeed report that the IBU nanoemulsion had a mean droplet size of 178.4 ± 9.0 nm, with a PDI of 0.27 ± 0.02, which is similar to the size of the FEN nanoemulsion (Figure 1b). A representative droplet size distribution for the IBU alginate nanoemulsion is shown in Figure 6e. The IBU drug loading in the shell of the dried particles was measured using a similar approach as described for the core. However, we did not precisely know the mass of the shell, so we used a volumetric approach to estimate the drug loading (Section S13, Supporting Information). We measured IBU shell drug loadings of 3.2%, 18.3%, and 26.3% by mass for each ϕ_{oil} loading level, demonstrating variable drug loading independent from the drug loading of the core (Figure 6f). We find for increasing ϕ_{oil} in the shell, d_{shell} does not noticeably change for hydrated particles: the linear best-fit has $R^2 = 0.22$ with $p = 0.77$, suggesting that the slope is not statistically different from 0. However, after the particles are

dried, d_{shell} increases significantly, due to the increased presence of IBU particles in the alginate matrix (Figure 6g).

2.6. Combination Particles Enable Tunable Sequential Drug Release

The solid-state of the IBU formulated in the alginate shell was characterized using the suite of solid-state characterization techniques used to characterize the core. Comparing the Raman spectra for bulk IBU and the composite shells at each loading level, we observe the characteristic peaks of IBU at 600, 780, 1168, 1258, 1615, 2900, and 3200 cm^{-1}, indicated with dashed-dotted lines in **Figure 7**a.[108] As shown by the DSC thermograms for the composite shells which do not exhibit a melting point, IBU is amorphous in the alginate matrix for all drug loading levels (Figure 7b). XRD patterns also support this conclusion (Figure S15a, Supporting Information). We can observe many amorphous IBU nanoparticles embedded in the alginate matrix through SEM (Figure 7c). We demonstrate that these IBU ASDs are kinetically stable and exhibit stable release performance over at least 10 months when stored in closed vials on the shelf at room temperature (Figure S16, Supporting Information). This is a promising timescale for ASD stability, indicating the potential scalability of this processing route to formulate ASDs.

We then tested the in vitro drug release performance of the dual-drug loaded core–shell particles. We find that varying the drug loading gives control for tuning the overlap between the release regimes of IBU (green curves) and FEN (blue curves), with

a varying degree of overlap between the release regimes of each drug (Figure 7d–f). For the low drug loading level (ϕ_{oil} = 0.01), the release regimes of the core and shell are completely separated, and all IBU is solubilized before FEN begins dissolving (Figure 7d). However, as the drug loading increases, the decreased density of the alginate matrix leads to faster matrix hydration and degradation, decreasing the separation between the release of IBU and FEN (Figure 7e). At the highest loading level (ϕ_{oil} = 0.21), the release windows of IBU and FEN are almost overlapping (Figure 7f). We observe this tunability of the overlap in the release windows since increasing the loading of IBU in the shell decreases the density of the alginate network, therefore accelerating the bulk hydration and erosion.

The demonstrated flexible sequential drug release and tunable loading in each layer suggest this technology could be scaled to manufacture FDC products, particularly when therapeutic molecules have competitive clearance mechanisms, are not compatible with the same excipient set, or are themselves chemically or physically incompatible. For example, repaglinide (anti-diabetic) and atorvastatin (anti-hyperlipidemia) treat comorbidities but exhibit competitive inhibition of the CYP3a4 clearance enzyme, and concomitant use could increase the risk of hypoglycemia.[109] Thus, formulating this combination in this core–shell platform with sequential release would decrease pill burden while minimizing adverse interactions. Structuring telmisartan and simvastatin, a synergistic combination proposed for coronary heart disease,[110] in separate layers could overcome the incompatibility of simvastatin with some excipients used in telmisartan formulations.[111] Other candidates could include a combination of antiretrovirals like zidovudine and efavirenz, which are commonly prescribed for the treatment of acquired immune deficiency syndrome (AIDS). Solid state incompatibilities have been reported between zidovudine and efavirenz,[112] suggesting that structuring each antiretroviral in distinct polymeric layers using this technology could be a promising formulation approach.

3. Conclusion

Here, we present the design of a novel, dual stimuli-responsive gelation process that exploits orthogonal thermoresponsive and ionotropic gel mechanisms to synthesize core–shell hydrogel particles with distinct hydrogel networks. We highlight the synergistic role Ca^{2+} plays in promoting the MC thermal gelation and the alginate ionotropic gelation, and the interplay between the salt-out effect and MC surface adsorption onto oil nanodroplet surfaces. We suggest that exploiting the salt-out effect could enable the development of thermal gelling processes at much lower temperatures than previously demonstrated, expanding the applicability of this approach to many APIs.

Core–shell particles are synthesized and used to encapsulate a FEN-loaded oil-in-water nanoemulsion. We confirm the presence of FEN nanocrystals and observe surface-adsorption of MC onto FEN nanocrystal surfaces. Particle geometry is characterized under varying process conditions, and we reveal the effect of particle geometry on resulting in vitro dissolution performance. The dissolution performance demonstrates strong release suppression and enables customizable, programmed dissolution of hydrophobic API. The dual gelation process is then adapted to

synthesize a combination product with IBU structured in the shell and FEN structured in the core. We demonstrate variable IBU loading in the shell and show sequential release of IBU and FEN from these particles. Finally, we show a 10-month stable alginate-IBU ASD in the particle shell. This dual gelation platform offers a potentially scalable approach to formulate hydrophobic APIs, target enteric or colonic disease orally, and manufacture FDC drug products with payloads structured in distinct polymeric layers. This approach can be generalized to other combinations of drugs, oil phases in the nanoemulsions, or thermo- and ionotropic-gelling polymers to make functional core–shell hydrogel particles.

4. Experimental Section

Materials: MC (viscosity: 15 cP, molecular weight ≈14 000 g mol^{-1}), sodium alginate (≈39% in guluronic acid blocks, M_w ≈ 100 kDa), FEN, anisole, Tween 80 (polysorbate 80), calcium chloride ($CaCl_2$), ethanol, sodium dodecyl sulfate, anhydrous disodium hydrogen phosphate (Na_2HPO_4), anhydrous monosodium hydrogen phosphate (NaH_2PO_4), mineral oil (ρ = 0.838 g mL^{-1}), and Nile red were purchased from Sigma-Aldrich and used without additional purification steps. IBU (99%, ACROS Organics) was purchased from Fisher Scientific and used without additional purification steps.

Drug-Loaded Dual-Responsive MC Nanoemulsions: The continuous and dispersed phases were first prepared separately before synthesizing the MC nanoemulsion. The continuous phase consisted of a 4 wt% MC aqueous solution. The dispersed phase consisted of saturated FEN-in-anisole solution, which was prepared by adding FEN into anisole until crystals crashed out of the solution. Next, the nanoemulsion was prepared by adding surfactant (Tween 80), the continuous phase, and the dispersed phase to a 50 mL Falcon conical centrifuge tube. The tube was sealed using Parafilm wax and the preemulsion was vortexed for 30 s. A 24 mm horn, 20 kHz ultrasonicator (from Cole Parmer) was used to prepare the nanoemulsion, using 20% amplitude for 30 min in a 30 s:10 s cycle at 10 °C. The temperature was controlled using a water circulator bath (from VWR). Following ultrasonication, $CaCl_2$ was dissolved in the nanoemulsion and mixed using a magnetic stir bar at 300 rpm until all of the $CaCl_2$ was dissolved. The formulation conditions for nanoemulsion synthesis are summarized in Table S1, Supporting Information.

Drug-Loaded Alginate Nanoemulsions: The continuous and dispersed phases were first prepared separately before synthesizing the alginate nanoemulsion. The continuous phase consisted of a 1 wt% alginate aqueous solution. The dispersed phase consisted of saturated IBU-in-anisole solution, which was prepared by adding IBU into anisole until crystals crashed out of the solution. Next, the nanoemulsion was prepared by adding Tween 80, the continuous phase, and the dispersed phase to a 50 mL Falcon conical centrifuge tube. The same ultrasonication procedure used to synthesize the MC nanoemulsions was used to synthesize the alginate nanoemulsions. The formulation conditions for nanoemulsion synthesis are summarized in Table S5, Supporting Information.

Dynamic Light Scattering: Dynamic light scattering (DLS) was performed using a Brookhaven NanoBrook 90Plus PALS at a fixed scattering angle of 90° and temperature of 25 °C. The sample was prepared by diluting 5 µL of nanoemulsion in 3 mL of DI water in a cuvette. Five sets of 1-min measurements were performed for each sample to characterize the droplet size distribution.

Rheological Characterization: The rheological properties of MC solutions and MC nanoemulsions were characterized using a stress-controlled rheometer (DHR-3, TA instrument). An upper-cone geometry (diameter = 60 mm, cone angle = 1.004°, and truncated gap = 29 µm) module. The sample was added into the sample holder on the lower Peltier steel plate, then the geometry was lowered to the truncated gap height. To minimize surface effects between MC and the geometry, the exposed edge of the

**ADVANCED
SCIENCE NEWS**

www.advancedsciencenews.com

**ADVANCED
HEALTHCARE
MATERIALS**

www.advhealthmat.de

cone was coated with mineral oil.[113,114] Water drops were added to the top of the cone geometry and a solvent trap was utilized to minimize solvent evaporation. A conditioning procedure was performed at 20 °C prior to each rheological measurement including a 60 s preshear at a constant frequency of 10 rad s^{-1} and a 60 s equilibration. The strain sweep experiment (Figure S1, Supporting Information) was performed at 25 °C, with a constant angular frequency (10 rad s^{-1}) at varying strain amplitude to determine an appropriate strain amplitude to use. The temperature ramp experiments were performed from 20 to 70 °C, at a strain amplitude of 5% and a frequency of 10 rad s^{-1}.

Dual Gelation Dripping Process: The dual gelation process was performed by dripping the dual gelation-capable nanoemulsion into a heated alginate bath. The bath consisted of 200 mL of 1 wt% alginate and 0.1% wt/v Tween 80 heated to 60 °C and stirred at 300 RPM. Tween 80 was added to decrease the surface tension of the bath and improve particle sphericity.[115] The nanoemulsion was loaded into a 3 mL syringe and dripped into the bath at a dripping height of 5 cm. The size of the dispensing tip used to extrude the nanoemulsion from the syringe was varied between 18 and 23 G to control particle size. The dual gelation process conditions for each formulation are summarized in Table S2, Supporting Information. The particles were left in the bath for 1 h for the alginate cross-linking to complete. Core–shell hydrogel particles were then harvested and the alginate cross-linking was quenched by diluting excess alginate in 1 L of DI water heated to 60 °C. The core–shell particles were subsequently placed on a non-stick baking pan, then placed in a 70 °C oven for solvent extraction and drug crystallization for 1 day. The resulting dried particles were stored at room temperature before performing further characterization.

X-Ray Diffraction: The crystalline structures of the drugs encapsulated in the composite particles were characterized with XRD using an in-reflection mode (Phillips PANalytical X'Pert Pro MPD). To prepare the sample, dried particles were harvested, and the core and shell were separated. The composite cores were crushed into a fine powder suitable for XRD analysis using a mortar and pestle and placed on a silicon crystal zero diffraction plate. The composite shells were similarly prepared. The diffraction angle 2-θ was swept from 4° to 40° by 0.0167° at a scanning rate of 2° min^{-1}. The equipment was operated at a constant voltage of 40 kV and a constant current of 40 mA.

Raman Spectroscopy: Raman spectroscopy was performed using a Horiba Jobin Yvon LabRAM HR800 system, using a 633 nm excitation laser, 100× objective lens, and 1800 lines per mm grating. Prior to measuring the Raman spectra, the core and shell of the composite particles were separated for measurement. Next, the system was calibrated using the standard 521 cm^{-1} band of Si. LabSpec 5 software was used to correct the spectra baseline using a line with a degree of two and identify peaks.

Differential Scanning Calorimetry: Thermal analysis of the as-received bulk drug and the composite drug-polymer matrices were analyzed using a differential scanning calorimeter (TA Instruments DSC 2500). The environment of the sample chamber was maintained as inert using a nitrogen gas flow at 50 mL min^{-1}. The sample was loaded into Tzero pans and lid with ≈10 mg of ground sample. First, the pan was equilibrated at −10 °C, then the pan was ramped to 150 °C at a heating rate of 10 °C min^{-1}. Finally, an isothermal step at 150 °C was held for 5 min.

Scanning Electron Microscopy: The solid-state morphology in the dried core–shell particles was observed using a high-resolution scanning electron microscope (Zeiss HRSEM) at 1 kV accelerating voltage and at a magnification of 30 000×. Samples were prepared on SEM specimen stubs with carbon tape. To improve contrast, SEM samples were coated with one layer of 10 nm gold nanoparticles.

Transmission Electron Microscopy: FEN nanocrystals and the surrounding MC matrix were observed using an FEI Tecnai G2 Spirit TWIN TEM equipped with a LaB6 filament, operating at an accelerating voltage of 120 kV. To prepare a suspension of FEN nanocrystals, ≈5 mg of composite MC-FEN core was crushed into a powder and dispersed in 200 µL of water. This suspension was then drop-cast onto carbon film-supported copper grids (size 200 mesh), and bright-field microscopy images were taken using a Gatan CCD camera. The resulting images were analyzed using ImageJ.

Drug Loading Characterization: The drug loading content of the composite core and shell were analytically characterized using UV–vis spectroscopy (ThermoFisher Scientific NanoDrop One/One^C Spectrophotometer). First, ≈10 mg of composite core or shell was crushed into a powder, then suspended in 3 mL of EtOH in a 10 mL Falcon centrifuge tube. The tube was vortexed, then allowed to settle. Next, 100 µL of the sample was diluted 10× into fresh ethanol to ensure that the concentration is in the linear spectrophonic regime. The sample's UV absorbance was measured at the appropriate λ_{max} (287 nm for FEN and 234 nm for IBU), the concentration was determined via a linear interpolation into the respective calibration curve, and the drug loading by mass was calculated from the concentration.

Cross-Polarized Microscopy: Cross-polarized microscopy (Zeiss Axiovert 5) was used to visualize the surface erosion of composite granules containing crystalline material from the composite MC-FEN core. A cross-polarized lens allowed for the visualization of birefringent domains in composite materials.[116] To facilitate surface erosion, 200 µL of 25 mM SDS was dripped onto the core.

Drug Release Experiments: The in vitro drug release of the dried core–shell particles was measured using a USP Dissolution Apparatus II (Agilent Technologies Varian VK 7025). A Cary 50 UV–vis spectrometer and an in situ probe set were integrated into the dissolution test in order to automatically record the absorbance at the λ_{max} for each drug (287 nm for FEN and 234 nm for IBU) each minute. The release media used was 900 mL of 25 mM SDS aqueous solution, according to the FDA guidance for dissolution methods for FEN from ref.[117]. For the IBU release tests, equivalency between 25 mM SDS and the FDA guideline of 50 mM PBS was established, and is shown in Figure S17, Supporting Information, in order to use the same release media for both drug tests. The vessel was operated at 37 °C and 75 rpm, and the drug concentration was set to 10 µg mL^{-1}. The release experiment for each particle formulation was performed in triplicate.

Statistics: The measurement uncertainty of mass measurements (0.01 mg) was propagated into the reported analytical drug loading calculations. The open-source model fitting package SciPy[119] was used to generate model fits when referenced. Linear least squares were used to optimize linear models, while non-linear least squares were used to optimize non-linear model fits.

Image Analysis: ImageJ[118] was used to analyze particle images to generate statistics on particle geometry. At least ten particles were imaged, and the mean and standard deviation are reported when referenced. Uncertainty was propagated from the standard deviation in these measurements in any calculations using particle geometry.

Supporting Information

Supporting Information is available from the Wiley Online Library or from the author.

Acknowledgements

Disclaimer

This report was prepared as an account of work sponsored by an agency of the United States Government. Neither the United States Government

Conflict of Interest

Data Availability Statement

The data that support the findings of this study are available from the corresponding author upon reasonable request.

Keywords

[1] T. Padhye, K. S. Maravajjala, K. L. Swetha, S. Sharma, A. Roy, *J. Drug Delivery Sci. Technol.* **2021**, *61*, 102178.

[2] V. B. Junyaprasert, B. Morakul, *Asian J. Pharm. Sci.* **2015**, *10*, 13.

[3] M. S. Alqahtani, M. Kazi, M. A. Alsenaidy, M. Z. Ahmad, *Front. Pharmacol.* **2021**, *12*, 618411.

[4] H. Liu, L. S. Taylor, K. J. Edgar, *Polymer* **2015**, *77*, 399.

[5] K. T. Savjani, A. K. Gajjar, J. K. Savjani, *ISRN Pharm* **2012**, *2012*, 195727.

[6] T. Vasconcelos, B. Sarmento, P. Costa, *Drug Discovery Today* **2007**, *12*, 1068.

[7] L. Schenck, D. Erdemir, L. Saunders Gorka, J. M. Merritt, I. Marziano, R. Ho, M. Lee, J. Bullard, M. Boukerche, S. Ferguson, A. J. Florence, S. A. Khan, C. C. Sun, *Mol. Pharmaceutics* **2020**, *17*, 2232.

[8] J. S. LaFountaine, J. W. McGinity, R. O. Williams 3rd, *AAPS PharmSciTech* **2016**, *17*, 43.

[9] A. Sosnik, K. P. Seremeta, *Adv. Colloid Interface Sci.* **2015**, *223*, 40.

[10] R. B. Hammond, K. Pencheva, K. J. Roberts, T. Auffret, *J. Pharm. Sci.* **2007**, *96*, 1967.

[11] P. Ganesan, D. Narayanasamy, *Sustainable Chem. Pharm.* **2017**, *6*, 37.

[12] Y. Xu, C. B. Michalowski, A. Beloqui, *Curr. Opin. Colloid Interface Sci.* **2021**, *52*, 101414.

[13] Z. H. Loh, A. K. Samanta, P. W. Sia Heng, *Asian J. Pharm. Sci.* **2015**, *10*, 255.

[14] B. E. Rabinow, *Nat. Rev. Drug Discovery* **2004**, *3*, 785.

[15] J. Stein, T. Fuchs, C. Mattern, *Chem. Eng. Technol.* **2010**, *33*, 1464.

[16] S. V. Bhujbal, B. Mitra, U. Jain, Y. Gong, A. Agrawal, S. Karki, L. S. Taylor, S. Kumar, Q. T. Zhou, *Acta Pharm. Sin. B* **2021**, *11*, 2505.

[17] F. Qian, J. Huang, M. A. Hussain, *J. Pharm. Sci.* **2010**, *99*, 2941.

[18] L. A. Sharpe, A. M. Daily, S. D. Horava, N. A. Peppas, *Expert Opin. Drug Delivery* **2014**, *11*, 901.

[19] J. Li, D. J. Mooney, *Nat. Rev. Mater.* **2016**, *1*, 16071.

[20] N. A. Peppas, J. Z. Hilt, A. Khademhosseini, R. Langer, *Adv. Mater.* **2006**, *18*, 1345.

[21] D. J. McClements, *Annu. Rev. Food Sci. Technol.* **2010**, *1*, 241.

[22] B. Baghaei, S. H. Jafari, H. A. Khonakdar, U. Wagenknecht, G. Heinrich, *J. Appl. Polym. Sci.* **2014**, *131*, 40625.

[23] D. Jagadeesan, I. Nasimova, I. Gourevich, S. Starodubtsev, E. Kumacheva, *Macromol. Biosci.* **2011**, *11*, 889.

[24] P. D. Godfrin, H. Lee, J. H. Lee, P. S. Doyle, *Small* **2019**, *15*, 1803372.

[25] A. Z. M. Badruddoza, A. Gupta, A. S. Myerson, B. L. Trout, P. S. Doyle, *Adv. Ther.* **2018**, *1*, 1700020.

[26] L.-H. Chen, P. S. Doyle, *Chem. Mater.* **2022**, *34*, 5194.

[27] L.-H. Chen, P. S. Doyle, *Adv. Mater.* **2021**, *33*, 2008618.

[28] T. Domenech, P. S. Doyle, *Chem. Mater.* **2020**, *32*, 498.

[29] H. B. Eral, M. O'Mahony, R. Shaw, B. L. Trout, A. S. Myerson, P. S. Doyle, *Chem. Mater.* **2014**, *26*, 6213.

[30] A. Z. M. Badruddoza, P. D. Godfrin, A. S. Myerson, B. L. Trout, P. S. Doyle, *Adv. Healthcare Mater.* **2016**, *5*, 1960.

[31] H. B. Eral, V. López-Mejías, M. O'Mahony, B. L. Trout, A. S. Myerson, P. S. Doyle, *Cryst. Growth Des.* **2014**, *14*, 2073.

[32] N. Sood, A. Bhardwaj, S. Mehta, A. Mehta, *Drug Delivery* **2016**, *23*, 748.

[33] R. Rodríguez-Rodríguez, H. Espinosa-Andrews, Z. Y. García-Carvajal, in *Functional Biomaterials: Drug Delivery and Biomedical Applications* (Eds: S. Jana, Ed., S. Jana), Springer Singapore, Singapore **2022**, pp. 75.

[34] X. Wan, P. Ma, X. Zhang, *Asian J. Pharm. Sci.* **2014**, *9*, 1.

[35] D. A. Sica, *Drugs* **2002**, *62*, 443.

[36] L. C. Luciani-Giacobbe, A. M. Lorenzutti, N. J. Litterio, M. V. Ramírez-Rigo, M. E. Olivera, *Drug Delivery Transl. Res.* **2021**, *11*, 894.

[37] T. Moulding, A. K. Dutt, L. B. Reichman, *Ann. Intern. Med.* **1995**, *122*, 951.

[38] T. L. Kauf, K. L. Davis, S. R. Earnshaw, E. A. Davis, *Patient Prefer Adherence* **2012**, *6*, 155.

[39] L. Oversteegen, M. Shah, H. Rovini, *Nat. Rev. Drug Discovery* **2007**, *6*, 951.

[40] S. Bangalore, G. Kamalakkannan, S. Parkar, F. H. Messerli, *Am. J. Med.* **2007**, *120*, 713.

[41] L. Dierickx, B. Van Snick, T. Monteyne, T. De Beer, J. P. Remon, C. Vervaet, *Eur. J. Pharm. Biopharm.* **2014**, *88*, 502.

[42] R. Fernández-García, M. Prada, F. Bolás-Fernández, M. P. Ballesteros, D. R. Serrano, *Pharm. Res.* **2020**, *37*, 132.

[43] M. Janczura, S. Sip, J. Cielecka-Piontek, *Pharmaceutics* **2022**, *14*, 834.

[44] D.-W. Kim, K. Y. Weon, *Int. J. Pharm. Investig.* **2021**, *51*, 555.

[45] T. Shams, M. Parhizkar, U. E. Illangakoon, M. Orlu, M. Edirisinghe, *Mater. Des.* **2017**, *136*, 204.

[46] A. Alzahrani, S. Narala, A. Adel Ali Youssef, D. Nyavanandi, S. Bandari, P. Mandati, A. Almotairy, M. Almutairi, M. Repka, *Eur. J. Pharm. Biopharm.* **2022**, *177*, 211.

[47] Y. Ding, S. Su, R. Zhang, L. Shao, Y. Zhang, B. Wang, Y. Li, L. Chen, Q. Yu, Y. Wu, G. Nie, *Biomaterials* **2017**, *113*, 243.

[48] S. Zu, Z. Zhang, Q. Liu, Z. Wang, Z. Song, Y. Guo, Y. Xin, S. Zhang, *Bio-Des. Manuf.* **2022**, *5*, 294.

[49] W.-H. Yin, C.-H. Zhou, X.-J. Ju, Y. Deng, L. Zhang, R. Xie, W. Wang, Z. Liu, L.-Y. Chu, *Colloids Surf., B* **2022**, *219*, 112806.

[50] B. C. Zarket, S. R. Raghavan, *Nat. Commun.* **2017**, *8*, 193.

[51] I. R. Wilding, S. S. Davis, F. Pozzi, P. Furlani, A. Gazzaniga, *Int. J. Pharm.* **1994**, *111*, 99.

[52] E. T. Cole, R. A. Scott, A. L. Connor, I. R. Wilding, H. U. Petereit, C. Schminke, T. Beckert, D. Cadé, *Int. J. Pharm.* **2002**, *231*, 83.

[53] A. Gazzaniga, P. Iamartino, G. Maffione, M. E. Sangalli, *Int. J. Pharm.* **1994**, *108*, 77.

**ADVANCED
SCIENCE NEWS**

www.advancedsciencenews.com

**ADVANCED
HEALTHCARE
MATERIALS**

www.advhealthmat.de

[54] M. A. Alhnan, T. C. Okwuosa, M. Sadia, K.-W. Wan, W. Ahmed, B. Arafat, *Pharm. Res.* **2016**, *33*, 1817.

[55] L. Zhang, J. Huang, T. Si, R. X. Xu, *Expert Rev. Med. Devices* **2012**, *9*, 595.

[56] J. Siepmann, N. A. Peppas, *Adv. Drug Delivery Rev.* **2001**, *48*, 139.

[57] D. Erdemir, T. Rosenbaum, S.-Y. Chang, B. Wong, D. Kientzler, S. Wang, D. Desai, S. Kiang, *Org. Process Res. Dev.* **2018**, *22*, 1383.

[58] W.-J. Sun, H. Chen, A. Aburub, C. C. Sun, *Powder Technol.* **2019**, *342*, 856.

[59] L. Shi, C. C. Sun, *Pharm. Res.* **2011**, *28*, 3248.

[60] M. L. Coughlin, L. Liberman, S. P. Ertem, J. Edmund, F. S. Bates, T. P. Lodge, *Prog. Polym. Sci.* **2021**, *112*, 101324.

[61] L. Li, P. M. Thangamathesvaran, C. Y. Yue, K. C. Tam, X. Hu, Y. C. Lam, *Langmuir* **2001**, *17*, 8062.

[62] J.-C. Arboleya, P. J. Wilde, *Food Hydrocolloids* **2005**, *19*, 485.

[63] D. K. Sarker, M. Axelos, Y. Popineau, *Colloids Surf., B* **1999**, *12*, 147.

[64] Z. Hu, R. Xu, E. D. Cranston, R. H. Pelton, *Biomacromolecules* **2016**, *17*, 4095.

[65] A. W. Chan, R. J. Neufeld, *Biomaterials* **2010**, *31*, 9040.

[66] J. R. Lakkakula, P. Gujarathi, P. Pansare, S. Tripathi, *Carbohydr. Polym.* **2021**, *259*, 117696.

[67] R. M. Lucinda-Silva, H. R. N. Salgado, R. C. Evangelista, *Carbohydr. Polym.* **2010**, *81*, 260.

[68] G. B. Messaoud, L. Sánchez-González, A. Jacquot, L. Probst, S. Desobry, *J. Colloid Interface Sci.* **2015**, *440*, 1.

[69] S. R. Banks, K. Enck, M. Wright, E. C. Opara, M. E. Welker, *J. Agric. Food Chem.* **2019**, *67*, 10481.

[70] H. H. Tønnesen, J. Karlsen, *Drug Dev. Ind. Pharm.* **2002**, *28*, 621.

[71] N. M. Velings, M. M. Mestdagh, *Polym. Gels Networks* **1995**, *3*, 311.

[72] K. Y. Lee, D. J. Mooney, *Prog. Polym. Sci.* **2012**, *37*, 106.

[73] D. S. Lima, E. T. Tenório-Neto, M. K. Lima-Tenório, M. R. Guilherme, D. B. Scariot, C. V. Nakamura, E. C. Muniz, A. F. Rubira, *J. Mol. Liq.* **2018**, *262*, 29.

[74] L. G. Gómez-Mascaraque, M. Martínez-Sanz, S. A. Hogan, A. López-Rubio, A. Brodkorb, *Carbohydr. Polym.* **2019**, *223*, 115121.

[75] M. Vogt, K. Kunath, J. B. Dressman, *Eur. J. Pharm. Biopharm.* **2008**, *68*, 283.

[76] Y. Kawabata, K. Wada, M. Nakatani, S. Yamada, S. Onoue, *Int. J. Pharm.* **2011**, *420*, 1.

[77] Y. Xu, C. Wang, K. C. Tam, L. Li, *Langmuir* **2004**, *20*, 646.

[78] Y. Xu, L. Li, P. Zheng, Y. C. Lam, X. Hu, *Langmuir* **2004**, *20*, 6134.

[79] K. Hayakawa, M. Kawaguchi, T. Kato, *Langmuir* **1997**, *13*, 6069.

[80] K. Yonekura, K. Hayakawa, M. Kawaguchi, T. Kato, *Langmuir* **1998**, *14*, 3145.

[81] A. Blandino, M. Macías, D. Cantero, *J. Biosci. Bioeng.* **1999**, *88*, 686.

[82] E.-S. Chan, B.-B. Lee, P. Ravindra, D. Poncelet, *J. Colloid Interface Sci.* **2009**, *338*, 63.

[83] J. Wu, T. Kong, K. W. K. Yeung, H. C. Shum, K. M. C. Cheung, L. Wang, M. K. T. To, *Acta Biomater.* **2013**, *9*, 7410.

[84] C. Chen, C. Gao, M. Liu, S. L., C. Yu, S. Ma, J. Wang, G. Cui, *J. Biomater. Sci., Polym. Ed.* **2013**, *24*, 1127.

[85] A. Heinz, K. C. Gordon, C. M. McGoverin, T. Rades, C. J. Strachan, *Eur. J. Pharm. Biopharm.* **2009**, *71*, 100.

[86] L. M. Dwyer, V. K. Michaelis, M. O'Mahony, R. G. Griffin, A. S. Myerson, *CrystEngComm* **2015**, *17*, 7922.

[87] S. Shikha, Y. W. Lee, P. S. Doyle, S. A. Khan, *Mol. Pharmaceutics* **2022**, *19*, 4345.

[88] P. L. Ritger, N. A. Peppas, *J. Controlled Release* **1987**, *5*, 37.

[89] V. Papadopoulou, K. Kosmidis, M. Vlachou, P. Macheras, *Int. J. Pharm.* **2006**, *309*, 44.

[90] K. Wang, H.-F. Wen, D.-G. Yu, Y. Yang, D.-F. Zhang, *Mater. Des.* **2018**, *143*, 248.

[91] P. Del Gaudio, G. Auriemma, P. Russo, T. Mencherini, P. Campiglia, M. Stigliani, R. P. Aquino, *Eur. J. Pharm. Biopharm.* **2014**, *87*, 541.

[92] S. Baumgartner, J. Kristl, F. Vrecer, P. Vodopivec, B. Zorko, *Int. J. Pharm.* **2000**, *195*, 125.

[93] B. N. Singh, K. H. Kim, *J. Controlled Release* **2000**, *63*, 235.

[94] S. S. Davis, J. G. Hardy, J. W. Fara, *Gut* **1986**, *27*, 886.

[95] D. Jain, R. Raturi, V. Jain, P. Bansal, R. Singh, *Biomatter* **2011**, *1*, 57.

[96] A. Maroni, L. Zema, M. Cerea, A. Foppoli, L. Palugan, A. Gazzaniga, *J. Drug Delivery Sci. Technol.* **2016**, *32*, 229.

[97] B.-B. C. Youan, *Adv. Drug Delivery Rev.* **2010**, *62*, 898.

[98] T. H. Baryakova, B. H. Pogostin, R. Langer, K. J. McHugh, *Nat. Rev. Drug Discovery* **2023**, *22*, 387.

[99] E. Mašková, K. Kubová, B. T. Raimi-Abraham, D. Vllasaliu, E. Vohlídalová, J. Turánek, J. Mašek, *J. Controlled Release* **2020**, *324*, 695.

[100] R. Vreeker, L. Li, Y. Fang, I. Appelqvist, E. Mendes, *Recent Adv. Food Sci.* **2008**, *3*, 361.

[101] R. Kumar, P. F. Siril, *AAPS PharmSciTech* **2018**, *19*, 284.

[102] T. B. Tierney, Y. Guo, S. Beloshapkin, Å. C. Rasmuson, S. P. Hudson, *Cryst. Growth Des.* **2015**, *15*, 5213.

[103] W. Zhu, F. S. Romanski, X. Meng, S. Mitra, M. S. Tomassone, *Eur. J. Pharm. Sci.* **2011**, *42*, 452.

[104] P. K. Jha, R. G. Larson, *Mol. Pharmaceutics* **2014**, *11*, 1676.

[105] Y. Ying, C. Beck, A. Wu, R. Dave, Z. Iqbal, *J. Raman Spectrosc.* **2017**, *48*, 750.

[106] W. Zhu, F. S. Romanski, S. V. Dalvi, R. N. Dave, M. Silvina Tomassone, *Chem. Eng. Sci.* **2012**, *73*, 218.

[107] E. H. Lee, *Asian J. Pharm. Sci.* **2014**, *9*, 163.

[108] W. F. Hug, Q. Nguyen, M. Reid, K. Sijapati, R. D. Reid, in *Next-Generation Spectroscopic Technologies XIII*, SPIE, Bellingham, WA **2020**, pp. 92–100.

[109] N. M. Pakkir Maideen, G. Manavalan, K. Balasubramanian, *Ther. Adv. Endocrinol. Metab.* **2018**, *9*, 259.

[110] M. Steinmetz, C. Brouwers, G. Nickenig, S. Wassmann, *J. Cell. Mol. Med.* **2010**, *14*, 1645.

[111] A. Kohlrausch, *US20060078615A1*, **2006**

[112] E. C. de, L. Gomes, W. N. Mussel, J. M. Resende, S. L. Fialho, J. Barbosa, M. I. Yoshida, *J. Braz. Chem. Soc.* **2013**, *24*, 573.

[113] D. Peressini, B. Bravin, R. Lapasin, C. Rizzotti, A. Sensidoni, *J. Food Eng.* **2003**, *59*, 25.

[114] J. D. dos Santos Carvalho, R. S. Rabelo, M. D. Hubinger, *Int. J. Biol. Macromol.* **2022**, *209*, 367.

[115] B.-B. Lee, P. Ravindra, E.-S. Chan, *Chem. Eng. Technol.* **2013**, *36*, 1627.

[116] A. Erfani, J. M. Schieferstein, P. Reichert, C. N. Narasimhan, C. Pastuskovas, V. Parab, D. Simmons, X. Yang, A. Shanker, P. Hammond, P. S. Doyle, *Adv. Healthcare Mater.* **2023**, *12*, 2202370.

[117] FDA **2021**.

[118] C. A. Schneider, W. S. Rasband, K. W. Eliceiri, *Nat. Methods* **2012**, *9*, 671.

[119] P. Virtanen, R. Gommers, T. E. Oliphant, M. Haberland, T. Reddy, D. Cournapeau, E. Burovski, P. Peterson, W. Weckesser, J. Bright, S. J. van der Walt, M. Brett, J. Wilson, K. J. Millman, N. Mayorov, A. R. J. Nelson, E. Jones, R. Kern, E. Larson, C. J. Carey, İ. Polat, Y. Feng, E. W. Moore, J. VanderPlas, D. Laxalde, J. Perktold, R. Cimrman, I. Henriksen, E. A. Quintero, C. R. Harris, et al., *Nat. Methods* **2020**, *17*, 261.